Significant Impact of Deprotonated Status on the Photoisomerization Dynamics of Bacteriophytochrome Chromophore

Haiyi Huang,[a,b] Chao Xu,*[b,c] Kunni Lin,[a,b] Jiawei Peng,[a,b] Feng Long Gu[b,c] and Zhenggang Lan*[b,c]

[a] School of Chemistry, South China Normal University, Guangzhou 510006, China

[b] MOE Key Laboratory of Environmental Theoretical Chemistry, South China Normal University, Guangzhou 510006, China

[c] SCNU Environmental Research Institute, Guangdong Provincial Key Laboratory of Chemical Pollution and Environmental Safety, School of Environment, South China Normal University, Guangzhou 510006, China

E-mail: zhenggang.lan@m.scnu.edu.cn; chaoxu@m.scnu.edu.cn

We report that the photoinduced dynamics of the phytochrome chromophore is strongly dependent on the protonation/deprotonation states of the pyrrole ring. The on-the-fly surface hopping dynamics simulations were performed to study the photoisomerization of different protonation/deprotonation phytochrome chromophore models. The simulation results indicate that the deprotonations at the pyrrole rings significantly modify the photoinduced nonadiabatic dynamics, leading to distinctive population decay dynamics and different reaction channels. Such feature can be well explained by the formation of the different hydrogen bond network patterns. Therefore, the proper understanding of the photoisomerization mechanism of phytochrome chromophore must take the hydrogen bond network into account. This work provides the new insights into the photobiological functions of phytochrome chromophore and suggests the possible ideas to control of its photoconversion processes for further rational engineering in optical applications.

Introduction

Phytochromes belong to a superfamily of photoreceptors responsible for fundamental photo-responses functions with biological significance, being widely found in plants and microorganisms.[1-4] They play crucial roles in a variety of light-regulated biological processes, ranging from seed germination, growth and flowering in plants to pigmentation and phototaxis in bacteria.[1, 5, 6] The phytochromes can be engineered into optical probes for deep-tissue imaging of living cells, thus their photochemistry is considerable significance for biomedical research and technology.[7-9]

The chromophores in phytochromes, as the photoreaction centers, are mainly classified as three categories, namely biliverdin (BV), phytochromobilin (PΦB) and phycocyanobilin (PCB). Their structures are very similar and all share a methane-bridged open-chain conjugated tetrapyrrole structures with differences on the two terminal rings (Scheme 1). Their basic photochemical reaction mechanism is the reversible photo- and thermal-conversions between two isomers, *i.e.* the red-absorbing form Pr and the far-red-absorbing form Pfr. The primary step of the Pr-to-Pfr photoisomerization mechanism is governed by the nonadiabatic transitions. Once red-light absorption at ~ 660 nm, the chromophore in Pr state undergoes an ultrafast *Z*-to-*E* photoisomerization accompanied by the internal rotation of pyrrole rings, then follows conformational relaxations and finally leads to the formation of the Pfr isomer via the thermal processes. The reverse Pfr-to-Pr conversion experiences the *E*-to-*Z* isomerization upon the photoexcitation with far red light at ~730 nm. The forward and backward isomerization reactions induce the large-sized conformational evolution of the whole photoreceptor protein, giving regulating signals to adjust relevant biological functions. Therefore, their photoinduced reactions have been extensively investigated experimentally and theoretically.[10-25]

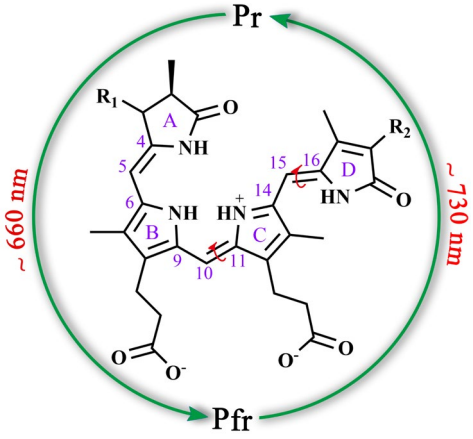

Scheme 1. Chromophores, photoreaction centers in phytochromes. (1) R_1: =CH-CH2-Cys, R_2: -CH=CH2 for BV; (2) R_1: -CH-(CH3)Cys, R_2: -CH2-CH3 for PCB; (3) R_1: -CH-(CH3)Cys, R_2: -CH=CH2 for PΦB.

Although numerous researches were conducted for many years, there are still several fundamental open questions in the photoinduced Pr-to-Pfr processes. The first critical argument is which molecular motion dominates the *Z*-to-*E* isomerization in the primary excited-state reaction. Several studies suggested

that in protein environments the photoisomization takes place around the $C_{15}C_{16}$ methine bridge, resulting in the torsion of nearly-free side Ring D along this bond.[11, 13, 26, 27] However, different isomerization mechanisms were also proposed. For instance, Ulijasz *et. al.* discovered that the internal rotation of the Ring A via the twisting motion of the C_4C_5 double bond triggers the excited-state dynamics of the PCB chromophore in photoreceptor protein.[21] It is also important to clarify the microscopic photoisomerization mechanism of the isolated chromophore at the all-atomic level. Some studies pointed out that the initial excited-state evolution of the isolated chromophore may be governed by the torsional motion at the $C_{10}C_{11}$ bond.[20, 28, 29] Zhuang *et. al* confirmed the pivotal role of the $C_{10}C_{11}$ double bond, and proposed that C_9C_{10} single bond is also an key rotational degree of freedom in the photoisomerization of the isolated PΦB chromophore.[20] The existence of different photoisomerization mechanisms for the isolated chromophore and chromophore in phytochrome protein pocket is possibly due to the geometrical constrains added by the interactions between the chromophore and the surrounding protein. In this sense, the deep understanding of the role of the protein pocket in the modification of the photoinduced dynamics of phytochrome chromophore still requires additional efforts. Furthermore, several works pointed out that the photochemistry of phytochrome chromophore is also strongly dependent on the hydrogen-bond network, as well as the protonation status of the pyrrole rings and surrounding residues.[16, 22, 30-34] A vibrational spectroscopic study on bathy phytochromes demonstrated that the proton transfer between the tetrapyrrole and a nearby histidine residue directly modules the photobiological functions by the generations of the photoactivated and deactivated states.[22] Osoegawa *et. al* revealed that the deprotonation of the Ring B/C distorts the methane bridge between the Ring B and the Ring C of the PCB chromophore, and such structural difference further adjusts the green or red light absorption.[33] Modi et. al clarified that the protonation/deprotonation status may regulate the light aborption of the BV chromophore in the protein pocket.[24] Kennis and co-workers proposed that the excited-state hydrogen transfer from the Ring A, B or C directly leads to the nonadiabatic decay to the ground state in the BV chromophore, resulting in the decreasing of the fluorescence signals.[30] Recently, Liu *et. al* demonstrated that the different orientations of the aspartate residue give the distinctive hydrogen-bond network connectivity that regulates the excited-state reaction channels.[16] As the summary, the protonation/deprotonation of the hydrogens attached to the pyrrole rings plays a critical role in the nonadiabatic dynamics of the phytochrome chromophore. It is interesting to clarify whether the removing of the hydrogen atom connected with the pyrrole nitrogen significantly modifies the nonadiabatic dynamics of the phytochrome or not. Particularly, it is also necessary to identify which key coordinates are responsible for the photoinduced dynamics of different phytochrome derivatives obtained by simple chemical modifications. These questions can be clearly addressed by the simulation of the nonadiabatic dynamics at all-atomic level, in which the active degrees of freedom in the excited-state dynamics are clarified by tracking the real-time molecular motion. In recent years, the on-the-fly *ab initio* nonadiabatic dynamics simulations were employed extensively to explore the ultrafast nonradiative reactions.[35-40] These simulations directly give the rich information, such as the time-dependent population dynamics, the nonadiabatic decay pathways and the essential molecular structure evolution.

In the present work, we wish to provide the detailed description of the photoisomerization of the isolated BV chromophore by using the on-the-fly nonadiabatic dynamics. The simulation was run with the trajectory surface hopping (TSH) approach[41] and the electronic structure calculations were performed at the semi-empirical OM2/MRCI level (the orthogonalization-corrected OM2 Hamiltonian combined with multireference configuration interaction).[42, 43] Many studied have verified that the nonadiabatic dynamics at the OM2/MRCI level is a powerful simulation tool in the description of excited-state processes for media-sized and large polyatomic systems with the balance of computational accuracy and efficiency.[44-49] By following the excited-state molecular motions, we found that the protonation/deprotonation states of the pyrrole ring show the strong impact on the excited-state lifetime and reaction pathways. The underline reason is that the hydrogen bond network deeply modules the intramolecular motion, leading to different profiles of excited-state potential energy surfaces. As the consequence, distinct population dynamics appear and different conical intersections are involved. Such finding confirms the important role of the hydrogen bond in the photoinduced nonadiabatic dynamics of the phytochrome chromophore. In other words, the understanding of the photoisomerization mechanism of phytochrome chromophere must take the hydrogen bond network into account, beside the steric effects caused by its surrounding protein environments. This work provides the new insights into the photobiological functions of phytochrome chromophere and suggests the possible ideas to control of its photoconversion processes for further rational engineering of near-infrared fluorescent proteins.

Computational details

The ground state minima (S_0_min) were optimized at the orthogonalization model 2 (OM2) level. The first excited state minima (S_1_min) and S_0/S_1 conical intersections (CI) were optimized at the OM2/MRCI level. The Lagrange-Newton algorithm was used for the conical-intersection optimization.[50, 51] At the semiempirical OM2/MRCI level, the active space includes 16 active electrons in 12 orbitals: six π orbitals, two *n* orbitals and four π^* orbitals. The OM2 Hamiltonian used the ROHF (restricted open-shell Hartree-Fock) approach in the construction of the reference orbitals, as this way provides the better description on the excited state wavefunctions. In the MRCI calculations, all electronic configurations in the Configuration Interaction scheme with the Graphical Unitary Group Approach (GUGA-CI) calculation were generated from five reference configurations, namely closed-shell, two single (HOMO-1 to LUMO and HOMO to LUMO), and two double

(HOMO-1 to LUMO and HOMO to LUMO) excitations, as shown in Figure S3-S6 in SI. We also performed the additional OM2/MRCI calculations with three reference configurations, namely closed-shell, single (HOMO to LUMO), and double (HOMO to LUMO) excitations for comparison. To examine whether the current active space is reasonable, we also try to build the excited-state reaction pathway by using the much large active space. All OM2/MRCI and OM2 calculations were performed by the MNDO 2020 package.[52]

The non-adiabatic dynamics for the four simplified BV chromophore models (**BV_N**, **BV_C**, **BV_B** and **BV_A**) with different protonation statuses were simulated by the on-the-fly trajectory surface hopping (TSH) approach at OM2/MRCI levels. The initial conditions of the nuclear coordinates and momenta were given by Wigner sampling of the lowest vibrational level on the electronic ground state.[53] The vertical excitation of all these samples into the first excited state defines the initial condition in the nonadiabatic dynamics. Here the lowest five electronic states were included in the TSH dynamics. All trajectories were propagated up to 2000 fs. The time steps in the propagation of the nuclear and electronic motion were 0.5 fs and 0.005 fs, respectively. The nuclear motion is integrated by velocity-Verlet method. The electronic propagation is conducted by the unitary propagation. The hopping probability is evaluated in the basis of Tully's fewest switches algorithm.[41] A practical way proposed by Granucci et. al was employed for the decoherence correction.[54] After hops, the velocities are corrected along the direction of the nonadiabatic coupling vectors for energy conservation. The frustrated hops were treated by reversing the velocity component along the nonadiabatic coupling vector.

Only for the **BV_N** model, when the 2000-fs nonadiabatic dynamics simulation is finished, we noticed that all trajectories return back to the ground states. Starting from these ending conditions in the phase space, the successive adiabatic dynamics on the electronic ground state was simulated by the 5000-fs Born-Oppenheimer Molecular Dynamics at the OM2 level.

The interface between the dynamics in the JADE package[36] and the electronic-structure calculations in the MNDO package were employed in all on-the-fly nonadiabatic and adiabatic dynamics simulations.

Results and discussion

We focus on the nonadiabatic dynamics of the Pr conformation of the BV chromophore in DrBphP (*Deinococcus radiodurans*) bacterial phytochrome. The ZsZsZa (C_5-Z, *syn* C_{10}-Z, *syn* C_{15}-Z, *anti*) stereoisomer (Figure S1 in Supporting Information (SI)) is chosen as our target configuration, which was identified as the dominant isomer by crystallography and NMR spectroscopy.[55-57] We built the simplified BV model to perform the nonadiabatic dynamics simulation, in which some side groups (-CH_2COO^- and -Cys-S) were replaced by hydrogen atoms to reduce the computational cost. As it is rather difficult to assign the protonation status by experimental studies, we consider all possible single deprotonation derivatives. In order to systematically rationalize the influence of phytochrome chromophore protonation state on the photoinduced processes, the four most probable protonation models (Figure 1 and Figure S2) were investigated, namely:

(1) **BV_N**: all nitrogen atoms protonated;

(2) **BV_C**: nitrogen in the Ring C deprotonated and the Rings A, B and D protonated;

(3) **BV_B**: nitrogen in the Ring B deprotonated and the Rings A, C and D protonated;

(4) **BV_A**: nitrogen in the Ring A deprotonated and the Rings B, C and D protonated.

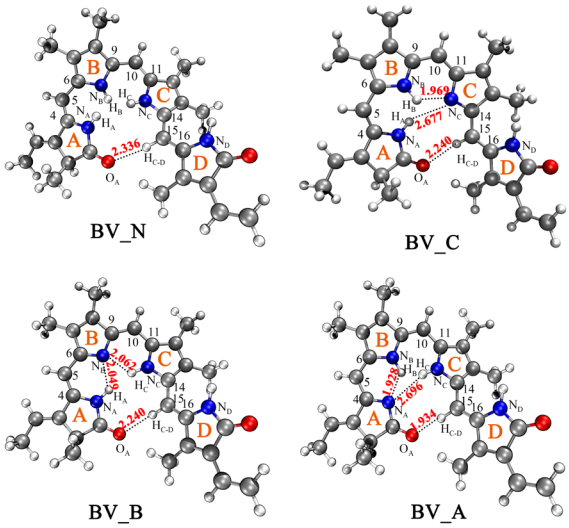

Figure 1. OM2 optimized S_0 minimum-energy structures of four most probable protonated BV-chromophore models. Selected bond lengths are given in Angstroms. See the Supporting Information for Cartesian coordinates.

We first optimized the structures of the S_0 and S_1 minima (S_0_min and S_1_min) for the four protonated/deprotonated BV chromophore models (**BV_N**, **BV_C**, **BV_B** and **BV_A**), and the key internal-coordinate parameters of these geometries are listed in Table S1-S4. The most striking feature here is that the different protonation patterns clearly build distinguishing hydrogen-bond networks, as shown in Figure 1 and Figure S7 in SI. For instance, at the S_0_min, only a weak hydrogen bond between O_A of the Ring A and H_{CD} atom (bridged the Ring C and the Ring D) is found in **BV_N**. However, the more complex hydrogen-bonding interactions are observed due to the presence of the multi-hydrogen-bond connectivity in the other three models (**BV_C**, **BV_B** and **BV_A**), as the results of the deprotonation of different pyrrole ring.

Figure 2 presents the time-dependent fractional occupations of the S_0 and S_1 electronic states for the above four models, assuming that all trajectories start from the S_1 state. Their lifetimes are far from each other and their corresponding time scales are even differed by the order of magnitude. The **BV_N** model with the saturated protonation displays the ultrafast excited-state population decay. The S_1 population decay to ~50% around 400 fs and the S_1 population becomes very low at about

1000 fs. As the contrast, the excited-state population decay of the **BV_C** model takes place at a much longer time scale and less than 50% of S_1 population decays to the S_1 state within 2.0 ps. The S_1 lifetimes of the latter two models (**BV_B** and **BV_A**) are extremely long and only the very minor population decay is observed within the simulation time duration. The remarkably distinctive population decay behaviors among these four BV models imply that their excited-state reaction mechanism may be drastically different. In this scenario, two open questions naturally arise: (i) how to explain the different population dynamics in these BV models and do they display different decay channels? (ii) how to correlate their decay mechanism and the protonation status? Next, we try to clarify both questions.

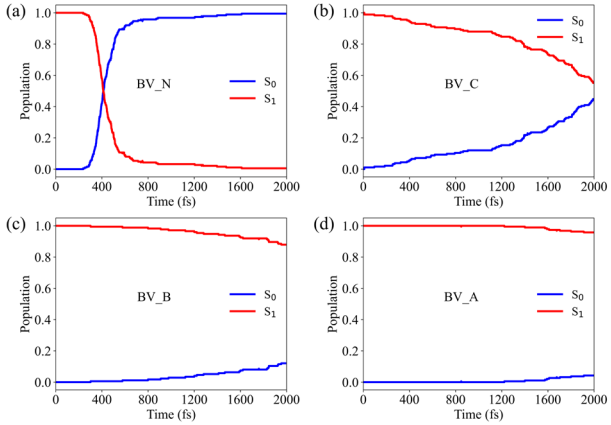

Figure 2. Time-dependent fractional occupations of the S_0 and S_1 electronic states of the four BV models (**BV_N**, **BV_C**, **BV_B** and **BV_A**) in the non-adiabatic dynamics staring from the S_1 state.

We begin with the **BV_N** model to explore the mechanism of the nonadiabatic dynamics. By analyzing all S_0/S_1 hopping geometries and the CI optimization results, we found that two S_0/S_1 minimum-energy conical intersections (CI_1 and CI_2 in Figure 3(a) and 3(b)) govern the nonadiabatic transitions. The former CI_1 is the main decay channel, since 93.6% trajectories decay via it, as shown in Figure 3(c).

The first conical intersection CI_1 is characterized by the strong twisting motion of the $C_{10}C_{11}$ bond, along with the minor torsion of the $C_{15}C_{16}$ bond. From S_0_min to CI_1, the dihedral angel of $C_9C_{10}C_{11}N_C$ between the Ring B and the Ring C changes from -12.4° to -85.4°, and the dihedral angel of $C_{14}C_{15}C_{16}N_D$ between the Ring C and the Ring D also changes slightly from 6.4° to 19.0°. For the trajectories via this channel, the rotation of whole C-D double-rings moiety takes place in the nonadiabatic dynamics, while the minor torsion of the terminal Ring D with respect to Ring C also exists.

The second conical intersection CI_2 is characterized by the significant twisting of the C_9C_{10} bond and also the minor torsion of the C_5C_6 bond. From S_0_min to CI_2, the dihedral angel of $N_BC_9C_{10}C_{11}$ between the Rings B and the Ring C increases from -16.5° to -93.4°, while the dihedral angel of $C_4C_5C_6N_B$ between the Ring A and the Ring B shows the minor decreasing from 28.2° to 17.6°. In this decay channel, the obvious rotation of the whole A-B double-ring moiety and the minor torsion of the terminal Ring A exist.

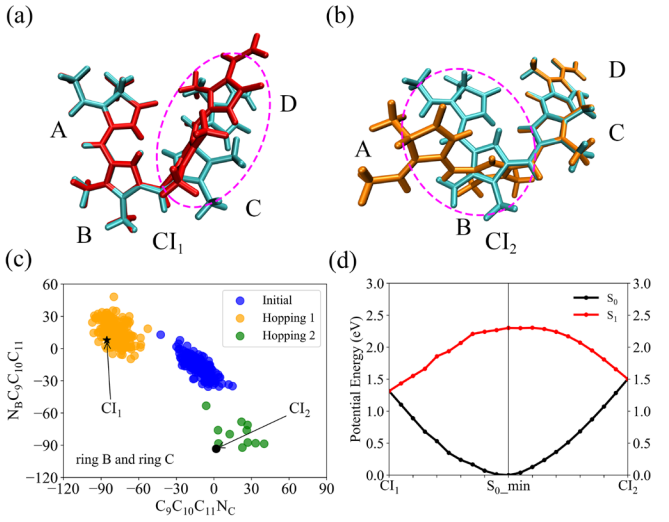

Figure 3. (a) and (b) OM2/MRCI optimized two S_0/S_1 conical intersections of the **BV_N** model. Cyan, red and gold represent S_0_min, CI_1 and CI_2, respectively. The CI_1 is characterized by the rotation of the whole C-D double-rings moiety around the $C_{10}C_{11}$ bond, while the CI_2 is featured by the rotation of the whole A-B double-rings moiety around the C_9C_{10} bond. (c) Distributions of two key dihedral angels at the initial and hopping geometries of the **BV_N** model. (d) Potential energy curves along the linear interpolated pathway from S_0_min to the two conical intersections CI_1 and CI_2 of the **BV_N** model.

The reaction pathways from the S_0_min to two conical intersections were built by employing the linear interpolated method. Figure 3(d) predicts that the CI_1 pathway should be more preferable, although both pathways are barrierless. Moreover, the S_1_min optimization directly gives the CI_1 geometry These findings clearly explain why the CI_1 channel is dominant in the nonadiabatic dynamics of the **BV_N** model (Figure 3(c)).

After the internal conversion of **BV_N**, the excessive kinetic energy leads to the high excitation of vibrational motions, and the system can easily overcome barriers on the electronic ground state to form various photoproducts. To explore possible reactions products, we ran the additional 5-ps Born-Oppenheimer molecular dynamics on the electronic ground state after the 2-ps nonadiabatic dynamics. By connecting the nonadiabatic and adiabatic dynamics, a few of representative trajectories are given in Figure 4. Starting from the S_1 state, the trajectories on the excited state move towards two S_0/S_1 CIs. Since the CI_1 channel is dominant, we mainly show the geometry evolution of some representative trajectories decaying via it. After the internal conversion back to the S_0 ground state, the initial **BV_N** isomer can be reformed though the reversed torsion of the whole C-D double-rings moiety, returning back to the starting **BV_N** configuration. Next, in some trajectories the vibrational energy flow may furtherly induce the internal rotation of the Ring D along the $C_{15}C_{16}$ bond, or the mixed Ring A and the Ring D rotations (Figure S8). At the

end of simulation, the ratio of these three channels is about 14.4%: 32.1%: 19.3%. Other isomers were also found while their probabilities are small (Figure S9). Since only 5.88% trajectories passing the CI_2, it is not necessary to discuss their final photoproducts. The current finding clearly confirms that the rotation of other rings (such as Ring D) may be highly possible even when such motion is not dominant in the excited-state dynamics. Nevertheless, such multiple-step reaction mechanism provides a possible explanation on why different isomerization patterns were discovered in previous studies.[11, 13, 20, 21, 26-29]

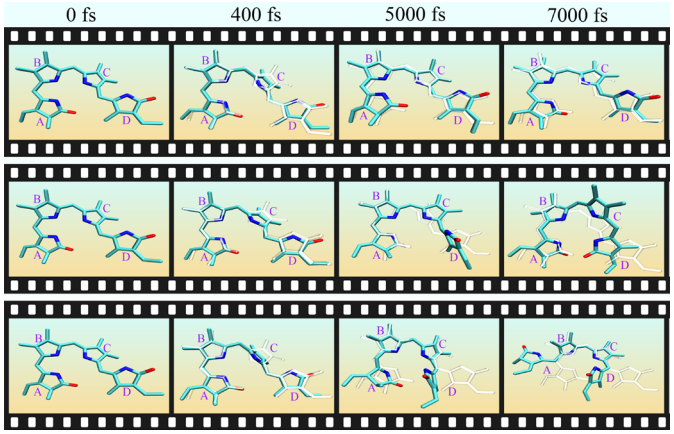

Figure 4. Representative trajectories towards to various reaction pathways. The cyan and white structural skeleton represent the snapshot at the current and starting time steps, respectively. Top: the trajectory back to initial **BV_N** structure; Middle: the trajectory ends with the rotation of the Ring D; Bottom: the trajectory evolution shows the mixed the Ring A and the Ring D rotations.

Next, let us consider the deprotonated **BV_C** model, which shows the longer excited state lifetime than the **BV_N** model (Figure 2). Different to **BV_N**, no significant torsional motion at the single and double carbon and carbon bonds between the Ring B and the Ring C was observed for **BV_C** in the trajectories. This difference can be understood by the presence of the strong hydrogen bond between deprotonated N_C and atom H_B in **BV_C**, which locks these torsional motions. As the consequence, the preferred isomerization pathways in **BV_N** are not observed in the excited-state dynamics of **BV_C**.

To clarify which motion is responsible for the nonadiabatic decay of the **BV_C** model, we collected the hopping geometries and located the key internal coordinates. As shown in Figure 5(a) and 5(b), two dihedral angels $N_CC_{14}C_{15}C_{16}$ and $H_BN_BC_6C_9$ are found to play the significant roles. Starting from these hopping geometries, the optimization of the minimum-energy S_0/S_1 CI geometry also confirms the importance of these two internal coordinates. Therefore, the synergy of the rotation of the Ring D and the out-of-plane motion of the H_B atom associated with the Ring B (H_BOOP) opens a new pathway in the nonadiabatic dynamics in the deprotonated **BV_C** model, different to the **BV_N** model.

The excited state reaction pathway of the **BV_C** model was given in Figure 5(c). Starting from Frank-Condon region, there is a barrierless pathway to the S_1_min. According to the linear-interpolated pathway from the S_1_min to the minimum-energy geometry in the S_0/S_1 CI (in Figure 5(d)), we noticed that the CI lies much higher than the S_1 minimum. Also considering the large size of the current chromophore, the vibrational relaxation on the excited state may lead to that the system tends to stay at the S_1 minimum region for very long time before it enters the CI region. This may explain the much slower nonadiabatic decay of the **BV_C** model with respect to the **BV_N** model. At the same time, this CI is accessible from the S_1_min only after the rather large geometrical adjustment on the excited state. Several motions must be involved, which include the significant H_BOOP motion ($\angle H_BN_BC_6C_9$ is 125.7° at CI, 159.9° at S_1_min and 176.9° at S_0_min), the breakdown of the strong hydrogen bond N_CH_B and the torsion of the $N_CC_{14}C_{15}C_{16}$ dihedral angel by ~10°. As the consequence, it takes a longer time for trajectories to access this CI region, resulting in the slow population decay of the **BV_C** model.

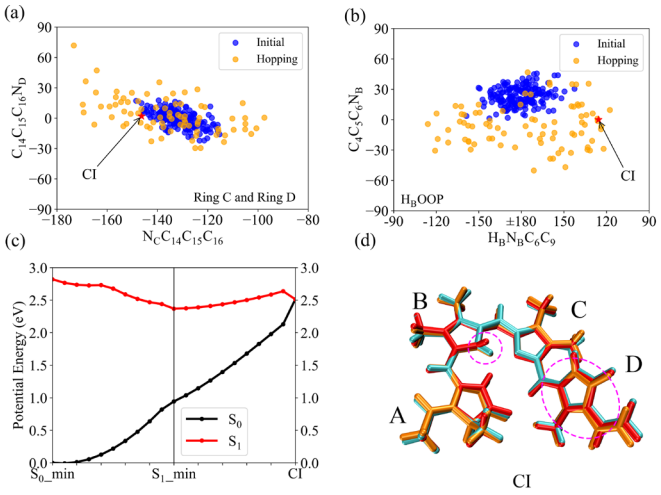

Figure 5. (a) and (b) Distributions of key dihedral angels at the initial and hopping points of the **BV_C** model. (c) Potential energy curves along the linear interpolated pathway from S_0_min to the S_1_min and from S_1_min to the CI for the **BV_C** model. (d) OM2/MRCI optimized S_0/S_1 CI of the **BV_C** model. Cyan, gold and red represent S_0_min, S_1_min and CI, respectively.

Now we pay attention to the deprotonated **BV_B** and **BV_A** models, which show significantly longer excited state lifetime (Figure 2). As the excited-state reaction pathways were clarified for **BV_N** and **BV_C** systems, it is necessary to examine whether these channels are possible in the **BV_B** and **BV_A** models.

In **BV_B** model, the hydrogen-bond network is observed clearly (see Figure S7). Similar to the **BV_C** case, the N_B-H_C hydrogen bond limits the torsional motion between the Ring B and the Ring C, preventing the ultrafast decay channel observed in the **BV_N** model. Meanwhile, the rotational motion of the Ring D is also blocked by the hydrogen bond between atom O_A and atom $H_{C\text{-}D}$. Moreover, as the nitrogen atom in the Ring B is deprotonated, there is no H_BOOP movement in this system. Therefore, **BV_B** cannot experience the similar decay channel as **BV_C**.

In **BV_A** model, the hydrogen bond between the Ring A and the Ring B freezes the rotation of $C_4C_5C_6N_B$. However, the twisting motion of the C_5C_6 bond is clearly involved in the early stage of the nonadiabatic dynamics for the **BV_N** model (see Figure S10), although the torsional motions at the bonds between the Ring B and the Ring C are dominant. As such torsional motion is fully locked in the **BV_A** model (see Figure S11), the corresponding channel is closed. In addition, the same hydrogen bond also restricts the H_BOOP motion of the Ring B, and the presence of the other strong hydrogen bond (S_1_min, $O_AH_{C\text{-}D}$ = 1.629 Å in Figure S7) prevents the torsional motion of the Ring D. Therefore, the decay pathway in the **BV_C** model cannot exist for the **BV_A** model.

Finally, we give some comments on the role of the hydrogen transfer in the nonadiabatic dynamics of the deprotonated **BV_C**, **BV_B** and **BV_A** models. Although the proton transfer may take place due to the existence of the hydrogen-bond network in the above three model (see Table S6 in SI), this motion is not important in the photoisomerization dynamics. Let us take the BV_C model with the highest nonadiabatic transition probability as an example, most hopping structures still remain as the BV_C configurations, and only 6.1% of them become the BV_B configurations. Even in this case, the existence of the hydrogen bond still locks the torsional motion at the single and double CC bonds between the Ring B and the Ring C. For the BV_A and BV_B models, the hydrogen transfer is also not important for the nonadiabatic decay dynamics and thus we do not repeat the discussions here. Overall, the proton transfer has very minor effects on the non-adiabatic transitions processes for the deprotonated models, possibly due to the fact that the overall hydrogen bond network is not destroyed after the proton transfer motion.

Conclusions

In this work, we employed the on-the-fly surface hopping dynamics simulation at the semiempirical OM2/MRCI level to understand the photoinduced processes for the BV phytochrome chromophore. Several critical geometries, including electronic state minima and conical intersections, were obtained. We found that the deprotonation of different pyrrole nitrogen leads to distinct photophysical and photochemical behaviors, such as the substantial changes in the excited state lifetime and nonadiabatic decay pathways.

The **BV_N** model shows the fastest excited-state decay because there are barrierless pathway from Franck-Condon region to the two CIs, and its excited-state process is dominated by the rotation of whole A-B double-rings moiety or whole C-D double-rings moiety. As the contrast, the excited-state population decay of the **BV_C** model takes place at a much longer time scale than that of **BV_N** model. The Ring D rotation and HOOP motion in the Ring B play efficient roles in the nonadiabatic process in the **BV_C** model. Interestingly, the other two models (**BV_A** and **BV_B**) show only extremely minor excited-state population decay within the simulation time duration.

We attribute the striking difference to the formation of different intramolecular hydrogen bond connective patterns, which affect the preferable reaction pathways and accessible conical intersections, and give diverse decay channels from the excited state to the ground state. At the end, we emphasize that in addition to the protein steric effect, the variation in deprotonation state also greatly impacts on the excited-state dynamics of the phytochrome chromophore. This finding not only deepens our understanding of the primary photoinduced reaction of the phytochrome chromophore, but also provides new design ideas for the efficient engineering near-infrared fluorescent proteins based on the phytochrome. Certainly, it is highly interesting to examine whether the protein environments can modify the protonation states of the BV chromophores and the protein pocket can regulate the photoisomerization dynamics. Such theoretical simulations may involve the further large scale QM/MM nonadiabatic dynamics simulations. This represents the challenging and on-going topic in the future study.

Author Contributions

H. Huang contributed to data curation, formal analysis, investigation, methodology, visualization and writing the original draft of the presented work. K. Lin and J. Peng contributed to data curation, formal analysis and methodology. C. Xu, F. L. Gu and Z. Lan contributed to methodology, project administration, funding acquisition, resources and supervision. All authors contributed to conceptualization of the project and review and editing of the manuscript.

Conflicts of interest

There are no conflicts to declare.

Acknowledgements

This work is supported by NSFC projects (No. 21903030, 21933011 and 21873112).

References

1 N. C. Rockwell, Y.-S. Su and J. C. Lagarias, *Annu. Rev. Plant Biol.*, 2006, **57**, 837-858.
2 Z. Yu and R. Fischer, *Nat. Rev. Microbiol.*, 2019, **17**, 25-36.
3 Y. Wang, G. Veglia, D. Zhong and J. Gao, *Sci. Adv.*, 2021, **7**, eabg3815.
4 C. Bongards and W. Gärtner, *Acc. Chem. Res.*, 2010, **43**, 485-495.
5 T. Kottke, A. Xie, D. S. Larsen and W. D. Hoff, *Annu. Rev. Biophys.*, 2018, **47**, 291-313.
6 W. R. Briggs and J. L. Spudich, 2005.
7 X. Shu, A. Royant, M. Z. Lin, T. A. Aguilera, V. Lev-Ram, P. A. Steinbach and R. Y. Tsien, *Science*, 2009, **324**, 804-807.
8 K. G. Chernov, T. A. Redchuk, E. S. Omelina and V. V. Verkhusha, *Chem. Rev.*, 2017, **117**, 6423-6446.
9 A. A. Kaberniuk, A. A. Shemetov and V. V. Verkhusha, *Nat. Method*, 2016, **13**, 591-597.

10 M. A. Mroginski, S. Adam, G. S. Amoyal, A. Barnoy, A. N. Bondar, V. A. Borin, J. R. Church, T. Domratcheva, B. Ensing and F. Fanelli, *Photochem. Photobio.*, 2021, **97**, 243-269.
11 M. A. Mroginski, D. H. Murgida and P. Hildebrandt, *Acc. Chem. Res.*, 2007, **40**, 258-266.
12 P. Altoe, T. Climent, G. C. De Fusco, M. Stenta, A. Bottoni, L. Serrano-Andrés, M. Merchán, G. Orlandi and M. Garavelli, *J. Phys. Chem. B*, 2009, **113**, 15067-15073.
13 X. Yang, Z. Ren, J. Kuk and K. Moffat, *Nature*, 2011, **479**, 428-432.
14 J. Dasgupta, R. R. Frontiera, K. C. Taylor, J. C. Lagarias and R. A. Mathies, *Proc. Natl. Acad. Sci. U. S. A.*, 2009, **106**, 1784-1789.
15 X. Xu, A. Höppner, C. Wiebeler, K.-H. Zhao, I. Schapiro and W. Gärtner, *Proc. Natl. Acad. Sci. U. S. A.*, 2020, **117**, 2432-2440.
16 X. Y. Liu, T. S. Zhang, Q. Fang, W. H. Fang, L. González and G. Cui, *Angew. Chem.*, 2021, **133**, 18836-18841.
17 D. Wang, Y. Qin, S. Zhang, L. Wang, X. Yang and D. Zhong, *J. Phys. Chem. Lett.*, 2019, **10**, 6197-6201.
18 D. Wang, X. Li, L. Wang, X. Yang and D. Zhong, *J. Phys. Chem. Lett.*, 2020, **11**, 8819-8824.
19 D. Wang, Y. Qin, M. Zhang, X. Li, L. Wang, X. Yang and D. Zhong, *J. Phys. Chem. Lett.*, 2020, **11**, 5913-5919.
20 X. Zhuang, J. Wang and Z. Lan, *J. Phys. Chem. B*, 2013, **117**, 15976-15986.
21 A. T. Ulijasz, G. Cornilescu, C. C. Cornilescu, J. Zhang, M. Rivera, J. L. Markley and R. D. Vierstra, *Nature*, 2010, **463**, 250-254.
22 F. Velazquez Escobar, P. Piwowarski, J. Salewski, N. Michael, M. Fernandez Lopez, A. Rupp, B. M. Qureshi, P. Scheerer, F. Bartl and N. Frankenberg-Dinkel, *Nat. Chem.*, 2015, **7**, 423-430.
23 B. Durbeej, O. A. Borg and L. A. Eriksson, *Chem. Phys. Lett.*, 2005, **416**, 83-88.
24 V. Modi, S. Donnini, G. Groenhof and D. Morozov, *J. Phys. Chem. B*, 2019, **123**, 2325-2334.
25 D. Morozov, V. Modi, V. Mironov and G. Groenhof, *J. Phys. Chem. Lett.*, 2022, **13**, 4538-4542.
26 J. Hahn, H. M. Strauss and P. Schmieder, *J. Am. Chem. Soc.*, 2008, **130**, 11170-11178.
27 Y. Yang, M. Linke, T. Von Haimberger, J. Hahn, R. Matute, L. González, P. Schmieder and K. Heyne, *J. Am. Chem. Soc.*, 2012, **134**, 1408-1411.
28 A. Strambi and B. Durbeej, *Photochem. Photobio. Sci.*, 2011, **10**, 569-579.
29 B. Durbeej, *Phys. Chem. Chem. Phys.*, 2009, **11**, 1354-1361.
30 K. Toh, E. A. Stojković, I. H. van Stokkum, K. Moffat and J. T. Kennis, *Proc. Natl. Acad. Sci. U. S. A.*, 2010, **107**, 9170-9175.
31 S. Bhattacharya, M. E. Auldridge, H. Lehtivuori, J. A. Ihalainen and K. T. Forest, *J. Bio. Chem.*, 2014, **289**, 32144-32152.
32 J. Zhu, D. M. Shcherbakova, Y. Hontani, V. V. Verkhusha and J. Kennis, *Sci. Rep.*, 2015, **5**, 1-8.
33 S. Osoegawa, R. Miyoshi, K. Watanabe, Y. Hirose, T. Fujisawa, M. Ikeuchi and M. Unno, *J. Phys. Chem. B*, 2019, **123**, 3242-3247.
34 O. Falklöf and B. Durbeej, *ChemPhotoChem*, 2018, **2**, 453-457.
35 R. Crespo-Otero and M. Barbatti, *Chem. Rev.*, 2018, **118**, 7026-7068.
36 L. Du and Z. Lan, *J. Chem. Theor. Comput.*, 2015, **11**, 1360-1374.
37 M. Barbatti, G. Granucci, M. Persico, M. Ruckenbauer, M. Vazdar, M. Eckert-Maksić and H. Lischka, *J. Photochem. Photobiol. A: Chem.*, 2007, **190**, 228-240.
38 S. Mai and L. González, *Angew. Chem.*, 2020, **59**, 16832-16846.
39 G. Cui and W. Thiel, *J. Chem. Phys.*, 2014, **141**, 124101.
40 B. F. Curchod and T. J. Martínez, *Chem. Rev.*, 2018, **118**, 3305-3336.
41 J. C. Tully, *J. Chem. Phys.*, 1990, **93**, 1061-1071.
42 A. Koslowski, M. E. Beck and W. Thiel, *J. Comput. Chem.*, 2003, **24**, 714-726.
43 W. Weber and W. Thiel, *Theor. Chem. Acc.*, 2000, **103**, 495-506.
44 A. Kazaryan, Z. Lan, L. V. Schafer, W. Thiel and M. Filatov, *J. Chem. Theor. Comput.*, 2011, **7**, 2189-2199.
45 T.-S. Zhang, Z.-W. Li, Q. Fang, M. Barbatti, W.-H. Fang and G. Cui, *J. Phys. Chem. A*, 2019, **123**, 6144-6151.
46 G. Cui and W. Thiel, *Angew. Chem.*, 2013, **125**, 451-454.
47 G. Cui, Z. Lan and W. Thiel, *J. Am. Chem. Soc.*, 2012, **134**, 1662-1672.
48 X. Pang, X. Cui, D. Hu, C. Jiang, D. Zhao, Z. Lan and F. Li, *J. Phys. Chem. A*, 2017, **121**, 1240-1249.
49 Z. Lan, E. Fabiano and W. Thiel, *J. Phys. Chem. B*, 2009, **113**, 3548-3555.
50 D. R. Yarkony, *Rev. Mod. Phys.*, 1996, **68**, 985.
51 T. W. Keal, A. Koslowski and W. Thiel, *Theor. Chem. Acc.*, 2007, **118**, 837-844.
52 W. Thiel, *Max-Planck-Institut für Kohlenforschung, Mülheim an der Ruhr, Germany*, 2020.
53 E. P. Wigner, in *Part I: Physical Chemistry. Part II: Solid State Physics*, Springer, 1997, pp. 110-120.
54 G. Granucci and M. Persico, *J. Chem. Phys.*, 2007, **126**, 134114.
55 J. R. Wagner, J. S. Brunzelle, K. T. Forest and R. D. Vierstra, *Nature*, 2005, **438**, 325-331.
56 X. Yang, E. A. Stojković, J. Kuk and K. Moffat, *Proc. Natl. Acad. Sci. U. S. A.*, 2007, **104**, 12571-12576.
57 J. R. Wagner, J. Zhang, J. S. Brunzelle, R. D. Vierstra and K. T. Forest, *J. Bio. Chem.*, 2007, **282**, 12298-12309.